ACS NANO

www.acsnano.org

ARTICLE

Programmable Multimodal Optothermal Manipulation of Synthetic Particles and Biological Cells

Hongru Ding, Zhihan Chen, Pavana Siddhartha Kollipara, Yaoran Liu, Youngsun Kim, Suichu Huang, and Yuebing Zheng*

Cite This: *ACS Nano* 2022, 16, 10878–10889

Read Online

ACCESS | Metrics & More | Article Recommendations | Supporting Information

ABSTRACT: **Optical manipulation of tiny objects has benefited many research areas ranging from physics to biology to micro/nanorobotics. However, limited manipulation modes, intense lasers with complex optics, and applicability to limited materials and geometries of objects restrict the broader uses of conventional optical tweezers. Herein, we develop an optothermal platform that enables the versatile manipulation of synthetic micro/nanoparticles and live cells using an ultralow-power laser beam and a simple optical setup. Five working modes (i.e., printing, tweezing, rotating, rolling, and shooting) have been achieved and can be switched on demand through computer programming. By incorporating a feedback control system into the platform, we realize programmable multimodal control of micro/nanoparticles, enabling autonomous micro/nanorobots in complex environments. Moreover, we demonstrate *in situ* three-dimensional single-cell surface characterizations through the multimodal optothermal manipulation of live cells. This programmable multimodal optothermal platform will contribute to diverse fundamental studies and applications in cellular biology, nanotechnology, robotics, and photonics.**

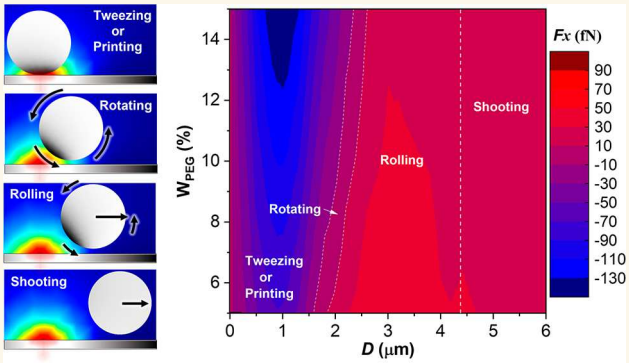

KEYWORDS: *optical manipulation, micro/nanorobots, multimodal manipulation, optothermal platform, single-cell manipulation*

Accurate manipulation of micro/nanoscale objects in a fluidic environment has attracted intensive interest and plays an important role in robotics, materials sciences, and life sciences.[1−3] Various manipulation techniques powered by light,[4,5] acoustic,[6] magnetic,[7] chemical,[8] and electric fields[9] have been developed. Among them, optical manipulation techniques such as optical tweezers show superior performance due to their remote and fuel-free control of synthetic particles and biological cells.[10,11] However, more efforts are needed to expand the manipulation modes of optical tweezers without increasing the optical setup complexity and to develop optical manipulation platforms into robotic systems that are capable of performing a wide range of tasks in an autonomous way. Currently, the limited working modes of optical tweezers hinder their applications in broader fields. For instance, in the biomedical field, micro/nanorobots with multiple working modes are highly desired, especially for nanosurgeries, in order to maintain high propulsion efficiency and carry out tasks in varying complex environments.[7] Nonetheless, most of the existing optical manipulation platforms exhibit only one type of locomotion modes: tweezing,[12−14] printing,[15,16] pushing,[17,18] pulling,[19,20] or rotation.[21−24] While several works have achieved dual-mode optical manipulation,[25,26] more manipulation modes being integrated into a single platform would be attractive for applications in automatous micro/nanorobots and multidimensional cell analysis.

The majority of the optical manipulation techniques demand complex optics and can only be applied to limited materials and geometries of objects. For example, most of the existing optical rotors[27] either demand asymmetric structures of rotors[28] or circularly polarized light[29] to sustain their rotation. Metallic nanorotors,[29] additional external fields,[23] or a vacuum environment[30,31] are often required to compensate for the weak light-matter interactions and driving forces at the

Received: March 29, 2022
Accepted: July 5, 2022
Published: July 11, 2022

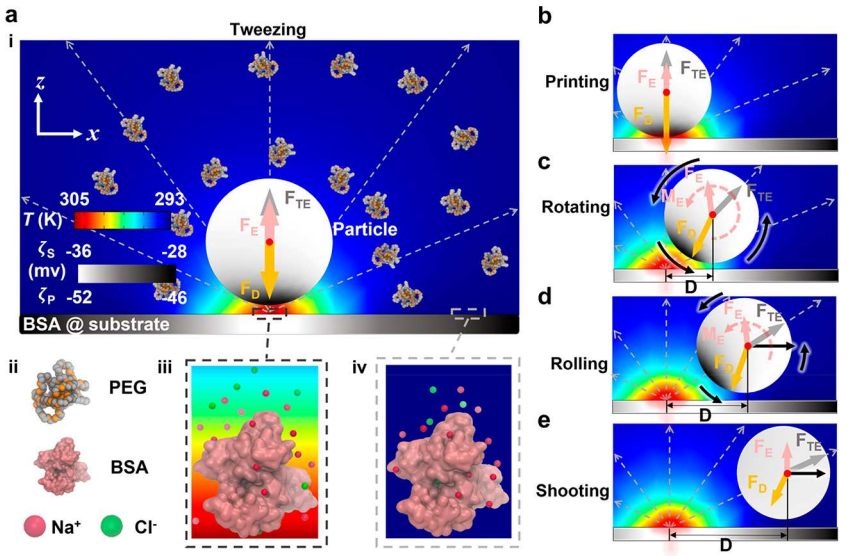

Figure 1. Working principle of multimodal optothermal manipulation platform. (a) Working principle of tweezing mode: In the nonuniform temperature field (i), PEG molecules, Na^+, and Cl^- ions (ii) diffuse to the cold region and generate concentration gradients. For clarity, only five temperature gradient lines (white dash arrows) are plotted to show the directions of the temperature gradient with the inset color bar (top) indicating the magnitude of temperature. The temperature field also affects the dissociation of carboxylic function groups, thus, a nonuniform surface charge on the particle, as shown in the inset color bar (bottom). The PEG concentration gradient leads to an unbalanced osmotic pressure and thus a downward depletion force, F_D, on the particle (yellow arrow). Differentiated concentration gradients of Na^+ and Cl^- ions, i.e., charge separation, generate an electric field and an outward thermoelectric force, F_{TE}, on the particle (gray arrow). Since BSA molecules have more charges in the higher temperature regions (iii and iv), a nonuniform surface charge occurs on the substrate as well, which exerts an outward electrokinetic force, F_E, on the particle (pink arrow). The particle is trapped in the hot region (tweezing mode) when F_D is larger than the sum of F_{TE} and F_E. (b) Printing of the particle is achieved by an enhanced F_D powered by a higher input laser power. We define the distance between the laser beam and the particle as D. When the particle is within a specific distance away from the laser spot, an electrokinetic torque (M_E) can also be generated (curved black arrow). Thus, by modulating the distance between the laser beam and the particle (i.e., increasing the D gradually), the particle can exhibit rotating (c), rolling (d), as well as shooting without any rotation (e), which stems from the direction and magnitude change of F_D, F_{TE}, and F_E. Optical intensity: 0.1 mW/μm^2.

nanoscale, which significantly constrains the rotors' applications. In some of the applications of optical tweezers, the tightly focused and high-power (10^2–10^3 mW) laser beams[32] could damage fragile targets such as biological cells.[33,34]

New strategies have been developed to tackle these challenges of optical manipulation. However, trade-offs among several desirable features are inevitable in most cases. For instance, Janus particles incorporating different light-absorbing components have been used to regulate dual-mode optical manipulation for the precise particle injection to living cells[35] and efficient particle delivery.[36] However, complex fabrication processes and multiple laser beams are required for the making and manipulation of the Janus particles. The operational optical power can be reduced by indirect manipulation,[37] photocatalytic reactions,[38] or plasmon-enhanced phoretic[12,14,18] or gradient force.[39] Nevertheless, these power-reducing strategies would also lower the spatial resolution, biocompatibility, or dynamics of the manipulation. Microfluid fields driven by optical rotors were harnessed to realize the translational motion of biological cells without photodamage.[40] However, the rotational motion (especially the out-of-plane rotation) of cells is often challenging[41] partially because of the intrinsic symmetry of cells suspended in an aqueous environment. Although out-of-plane cellular rotation has been lately achieved at the optical trap generated by two laser beams,[42] the high optical power, low manipulation dynamics, and low throughput largely limit the further development of the platform for practical applications.

Herein, through the synergy of thermoelectric (TE) force, depletion force, and electrokinetic interactions, we developed a multimodal and universal micro/nanomanipulation platform where biological cells and synthetic colloidal particles with different materials and sizes can be manipulated in diverse modes, including printing, tweezing, rotating, rolling, and shooting. The switching of the different modes can be realized by simply tuning the laser-object distance or optical power. Moreover, the platform features low operational power, programmability, and single-object resolution, which enable noninvasive and precise optical manipulation for a wide range of applications. As initial demonstrations of the applications, we employ the manipulation platform to realize multimodal micro/nanorobots and multidimensional single-cell analysis.

RESULTS AND DISCUSSION

General Concept. We develop a multimodal manipulation platform to enable on-demand control of translational and rotational motions of colloidal micro/nanoparticles and biological cells with force fields modulated by a laser-generated temperature gradient. The key concept of the platform is shown in Figure 1. Upon the illumination of a laser beam on a light-absorbing substrate coated with a thin layer of bovine serum albumin (BSA), a nonuniform temperature field is generated within a few microseconds near the laser spot in polyethylene glycol (PEG)/phosphate-buffered saline (PBS) solution, where micro/nanoscale objects can be manipulated in a variable fashion via the synergy of depletion force (F_D), thermoelectric force (F_{TE}), and electrokinetic force (F_E)

https://doi.org/10.1021/acsnano.2c03111
ACS Nano 2022, 16, 10878–10889

(Figure 1a(i)). Specifically, F_D stems from the hot-to-cold thermophoretic motions of PEG molecules. The generated concentration gradient leads to a nonuniform osmotic pressure on the surface of particles, which pushes the particle toward the hot region.[43,44] In addition, the Na^+ and Cl^- ions from the PBS solution also possess the hot-to-cold thermophoretic motions, but with different drift velocities ($v_{Na^+} > v_{Cl^-}$). The resulting different spatial distributions of two counterions produce a thermoelectric field (i.e., TE field) that points to the hot center along the direction of the temperature gradient (Supplementary Figure 1), which would repel the negatively charged objects away from the hot spot based on F_{TE}.[14,45,46] Moreover, the BSA-coated substrate features a negative surface zeta potential, which leads to the F_E that drive any negatively charged objects away from the hot spot as well.

The synergy of F_D, F_{TE}, and F_E can be tailored by laser-particle distance and laser power due to the strong temperature dependence of the three forces. Specifically, dominated by the thermal diffusion of molecules and ions, the magnitude of F_D and F_{TE} increases with the temperature gradients.[14,43] Meanwhile, F_E can also be controlled by the temperature field since the surface charge of BSA is sensitive to temperature. As illustrated by the grayscale image of the substrate in Figure 1a(i), the hot region of the BSA-coated substrate possesses a higher surface zeta potential because the primary structure of BSA with negative charges is exposed to the solution[47,48] (Figure 1a(iii-iv)). The measured zeta potentials and surface zeta potentials at different temperatures can be found in Supplementary Note 1. In addition to the magnitude of each force, their directions can also be tuned on-demand by simply controlling the distance between the laser beam and target particles (D). Accordingly, through adjusting optical density and D, we have successfully achieved a multimodal micro/nanomanipulation platform, in which the effective conditions of different working modes are introduced below:

Tweezing Mode. The objects are trapped and achieve in-plane movement on the substrate. When the incident laser beam illuminates the center of the object (i.e., $D = 0$), the three forces are all exerted along z axis with negligible torques (as depicted in Figure 1a). By continuously moving the position of the laser, the object can follow the laser beam and be transported freely.

Printing Mode. By simply increasing the optical power in the setup of tweezing mode, the trapped particle can be immobilized on the substrate (as shown in Figure 1b). An increasing thermodiffusion of PEG molecules leads to an enlarged downward net force that stabilizes the target particle at the beam spot with a small particle-substrate gap. A strong entropy-driven depletion of PEG molecules, thus, occurs at the particle-substrate interface, exerting a higher osmotic-pressure imbalance on the object.[49] When the depletion force dominates over the electrostatic repulsion, the object comes into closer contact with the substrate, which initializes the van der Waals interaction and makes the object immobilized on the substrate.

Rotating Mode. The object can also achieve out-of-plane rotation without translational motions in the vicinity of the laser spot, which requires an intermediate value of D (Figure 1c). Since the surface charge on many synthesized particles and biological cells (e.g., fungi,[50] bacteria,[51] and human cells[52]) with ionized acid groups is nonuniform under the nonuniform temperature field,[53,54] the line of action of F_E does not pass through the centroid of the particles or cells. Therefore, F_E can be decomposed into a force passing through the centroid of the particle and a torque (M_E) that drives the rotation (see Supplementary Note 2 for the visualization of the discrete F_E force). By placing the laser at a suitable D, a force balance among the three forces can be attained while the electrokinetic torque (M_E) powers a steady rotation.

Rolling Mode. Rolling, combined rotational and translational motion of the object, can be achieved when D is further increased (Figure 1d). Here, the angle between x axis and the temperature gradient line passing through the centroid of the particle (i.e., the direction of F_{TE}) becomes smaller, leading to an increment of the x component of F_{TE}. The particle, thus, experiences a net force along x axis that drives the particle to move away from the hot region. Note that the particle rotates at a relatively slower rate compared to the rotating mode owing to the smaller M_E as the temperature gradient decreases.

Shooting Mode. Moreover, the object can show fast in-plane translational motions away from the hot spot with negligible rotational motions when D is larger than a critical value (Figure 1e). At a location far away from the laser spot, the nonuniformity of the surface charges on the particle and substrate becomes trivial. An electrokinetic force from the substrate passes through the centroid of the particle and the torque vanishes. The net force along x axis acts on the particle, shooting the particle toward the cold region.

Modeling and Rational Design. To validate and rationally design the proposed multimodal platform, we performed force analysis on a 2.8 μm polystyrene (PS) particle that possesses negative zeta potential and works at the different modes through a multiphysics model based on finite element analysis (FEA) and finite-difference time-domain (FDTD) simulations (see the Methods for simulation details). The optical intensity was set as 0.1 mW/μm^2. The opto-thermal forces (F_{TE}, F_D, and F_E) and torque (M_E) on the particle were calculated (see Supplementary Note 2 for more details). The depletion force is defined as $F_D = -\oint c k_B T \, dA_r \hat{n}$ (c: local PEG concentration, k_B: Boltzmann constant, T: local temperature, dA_r: differential area element on the particle surface, $\hat{n}$: unit vector normal to the particle surface). TE force was obtained by the integration of parallel components of the TE field at the rotor surface: $F_{TE} = \oint \sigma_r E_{TE,\parallel} \, dA_r$ (σ_r: surface charge density of the particle, $E_{TE,\parallel}$: tangential component of the TE field along the particle surface). Electrokinetic force is given as $F_E = \oint \sigma_r \, dA_r \int_{x\to-\infty}^{x\to\infty} \int_{y\to-\infty}^{y\to\infty} E_\parallel$ ($E_\parallel$: parallel component of the electric field from the substrate). Stemming from thermophoresis of molecules and ions, F_D and F_{TE} are dominated by the temperature field of the surrounding liquid. Moreover, F_E is also temperature-dependent because the surface charges of the substrate and particles are both sensitive to temperature. Considering that the laser-modulated temperature gradient is nonuniform (Supplementary Figure 2), three opto-thermal forces as well as the electrokinetic torque (defined by $M_E = \oint a\hat{n} \times dF_E$) significantly vary with the laser-particle distance, D.

To quantitatively analyze the occurrence of different modes, we decouple the translational and rotational motions, the former of which is determined by the x components of F_{TE}, F_D, and F_E and the latter of which is only related to M_E around the y-axis. For the translational motions, $F_{TE,x}$ and $F_{D,x}$ have similar magnitude but opposite sign (Supplementary Note 2), while $F_{E,x}$ is 2 orders of magnitude smaller than the other two forces.

https://doi.org/10.1021/acsnano.2c03111
ACS Nano 2022, 16, 10878−10889

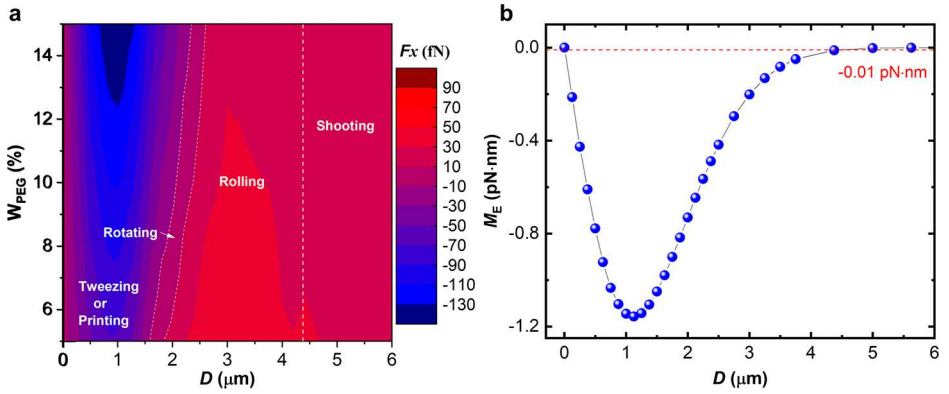

Figure 2. Phase diagram and force analysis of multimodal manipulation. (a) Simulated phase diagram showing the different manipulation modes of a 2.8 μm PS particle and demonstrating the relationship among the net force along the x axis on the particle (F_x), laser-particle distance (D), and PEG concentration (W_{PEG}). F_x turns into a positive value from the negative as D increases. (b) Simulated electric torque (M_E) from the substrate, which governs the rotational motion, as a function of D. The red dashed line marks the critical D value (4.38 μm), exceeding when M_E is close to zero. The full-dimensional particle motion can be predicted by these two figures. The working regions of each mode can be outlined by the white dashed lines in (a).

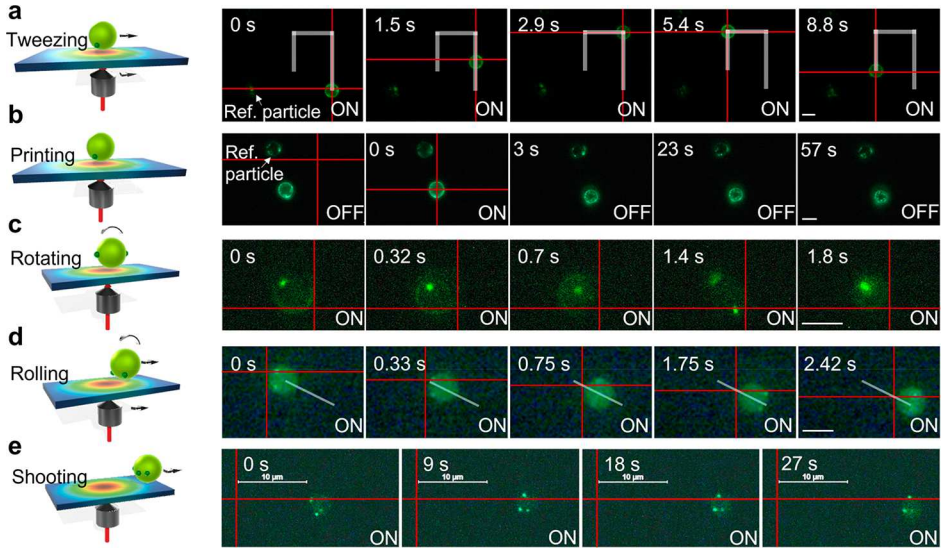

Figure 3. Experimental demonstration of multimodal manipulation of microparticles. (a) Schematic (left) and successive fluorescence (right) images of a trapped 2.8 μm PS particle (labeled by fluorescent nanobeads) being transported along a designed path. "ON" and "OFF" indicate that the laser beam is turned on and off, respectively. (b) Schematic and successive fluorescence images showing the particle printing process. Once printed, the target particle showed no Brownian motion, while the reference particle showed obvious random movements according to the motions of nanobeads on the particles' surface. (c) Schematic and successive fluorescence images showing the particle rotating process as the laser beam was moved away from the particle. (d) Schematic and successive fluorescence images showing the rolling process. The gray line corresponds to the designed translation path. (e) Schematic and successive fluorescence images showing the shooting process. Scale bars: (a)−(d) 3 μm; (e) 10 μm.

Note that the optical force on the particle is always negligible in our system (~1 fN) due to the low optical power intensity (Supplementary Figure 3). Therefore, the x component of the net force can be safely simplified to $F_x = F_{TE,x} + F_{D,x}$. Then we depicted the sign and magnitude of F_x in Figure 2a in terms of the two most important parameters, laser-particle distance D and concentration of PEG. Identical with our experimental observation, F_x was found to change its sign when D is ~1.58−1.83 μm, where this critical value is changed with the weight percentage of PEG molecules. Such a change originates from the change of PEG concentration gradient, which leads to a varying $F_{D,x}$ (Supplementary Note 2). For instance, at a 5% PBS solution with 5% PEG molecules, F_x functions as an attractive force when D is smaller than 1.58 μm, and the particle will finally be trapped or printed in the laser spot with $D = 0$ (Figure 2a). Rotating mode can be achieved by increasing D to a certain range (1.58 μm < D < 1.83 μm) where F_x is around zero, leading to zero translation momentum. Interestingly, in this range of D, the electrokinetic torque almost reaches the maximum value, which favors the rotational motions of the particle (Figure 2b). By further increasing D to be larger than 1.8 μm, F_x turns into a positive force that propels the particle from the hot region to the cold region, because the repulsive $F_{TE,x}$ starts dominating in the regime instead of the attractive $F_{D,x}$. It is worth noting that M_E can decrease close to zero when the particle is distant from the hotspot (Figure 2b). At a large D, the temperature gradient of the surrounding environment declines, which alleviates the nonuniformity of both substrate and particle surface charges. Therefore, M_E is reduced due to the decrease of F_E. Suppose

https://doi.org/10.1021/acsnano.2c03111
ACS Nano 2022, 16, 10878−10889

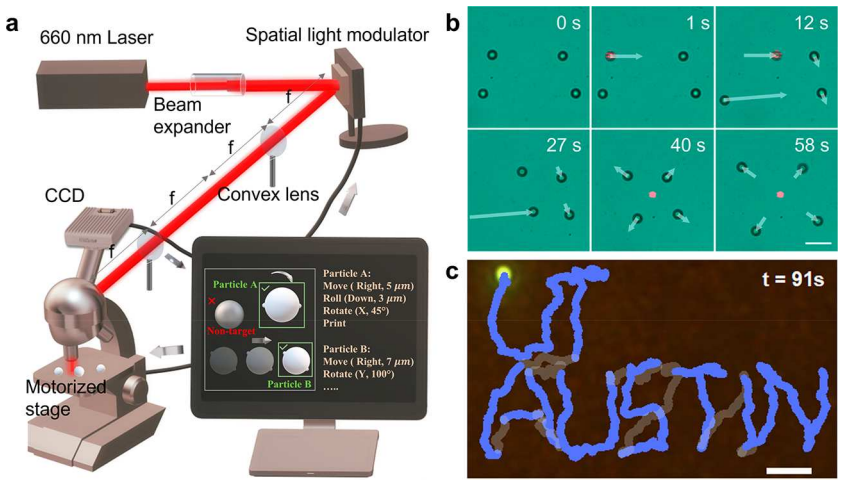

Figure 4. Automated manipulation of micro/nanoparticles with feedback control. (a) Optical setup of the automated manipulation system with feedback control. (b) Time-resolved images of dynamic patterning using four PS microparticles. (c) A 200 nm Au nanosphere moves along a predesigned path to finish the writing of a "UT AUSTIN" pattern in 91 s (as shown by the dark-field optical imaging). The gray lines show the transition trajectories among different letters. Scale bars: (b) 5 μm; (c) 1 μm.

that the particle is deemed not to rotate when M_E decreases to 2 orders of magnitude smaller than the maximum (1.16 pN·nm). Consequently, the particle displays the rolling mode as 1.83 μm < D < 4.38 μm and the shooting mode at D > 4.38 μm. F_D, F_{TE}, F_E, M_E, and critical D values increase with particle size due to the increment of surface area. For large particles (>10 μm), F_D can reach 8 pN (Supplementary Note 2). Thermo-osmosis flow from the substrate is negligible here because of the highly charged substrate and the thick chamber.[55−57] We also note that the thermophoretic motion induced by the thermo-osmotic salt-ion flow around particles is trivial compared to the thermoelectric effect in electrolyte solutions with large Seebeck coefficients such as PBS herein.[58−60]

Multimodal Manipulation of Microparticles. The 2.8 μm PS microparticles with carboxylic functional groups on the surface were dispersed in a 5% PBS solution with 10% PEG molecules to experimentally validate our physical model (Figure 2) and demonstrate the capability of our platform for on-demand versatile multimodal manipulation of single particles. To observe the rotational motion of particles, we labeled the PS microparticles with 40 nm fluorescent beads through streptavidin−biotin binding. A thin layer of BSA proteins was coated on a glass substrate predeposited with gold nanoislands (AuNIs) (see the Methods for fabrication details and Supplementary Figure 4 for a scanning electron micrograph). A 660 nm laser beam with low power intensity (I), 0.05−0.3 mW/μm^2, was used to generate the temperature gradient fields (see Supplementary Note 3 for temperature measurements) for the manipulation of micro/nanoparticles and biological cells in this work.

As shown in Figure 3a (also Supplementary Movie 1), a PS bead was trapped using a laser beam (I = 0.06 mW/μm^2; D = 0 μm) and dynamically transported along a designed path at a velocity of ∼5 μm/s. The manipulation efficiency (translation velocity divided by optical intensity) of the tweezing mode in this platform reaches ∼80 μm^3/(mW·s), which is 1−2 orders of magnitude higher than that of optical tweezers and is comparable to that of opto-thermoelectric tweezers.[14] In our system, the Brownian motion of particles is at least 16 times smaller than that of the particles suspended in pure water, owing to the viscous PEG/PBS solution[61] and the small particle-substrate distance.[62] The trapping stiffness ranges from 11.3 to 22.0 pN/μm at variable optical intensities from 0.25 to 0.75 mW/μm^2 (see Supplementary Figure 5). Interestingly, the printing of the PS microparticle onto the substrate can be achieved at a higher temperature gradient by simply increasing I to >0.2 mW/μm^2 with D at 0 μm (see Figure 3b(ii) and Supplementary Movie 2). The gap between the trapped particle and the substrate is reduced owing to the larger F_D, resulting in the entropy-driven depletion of the PEG molecules at the particle−substrate interface (Supplementary Figure 6). The unbalanced osmotic pressure on the particle's surface is thus enhanced, adding on a downward force. The addition of depletion attraction to the bonding force makes our platform stand out as a low-power optical printing technique in comparison with most existing optical printing techniques.[16] As shown in the successive fluorescent images, the Brownian motion of the target particle completely vanished when the laser was turned off. In stark contrast, the reference particle displayed obvious random fluctuations in its position (notice the position change of fluorescent beads on the reference particle), further proving the immobilization of the PS particle.

Predicted by our model, the rotating mode (Figure 3c and Supplementary Movie 3) was achieved by placing the laser beam about 1.6 μm away from the particle, i.e., D = ∼ 1.6 μm. A rotation rate of 23.2 rpm was obtained at I equal to 0.16 mW/μm^2. Of note, an out-of-plane rotation, i.e., the rotation axis parallel to the substrate, is achieved in our platform, which has been proven extremely challenging to be implemented via any other optical manipulation methods.[63] Conventional optical rotor systems typically require laser beams with complex intensity profiles and polarizations, or rotors with sophisticated shapes or material birefringence so that an optical torque can be generated to power their rotation.[27] In contrast, our rotating robots can be sphere-symmetric and isotropic and function with a low-power and simple optical setup.

As D was further increased to 1.9 μm, the PS particle worked in the rolling mode (Figure 3d and Supplementary Movie 4), which is also consistent with our prediction shown in Figure 2. In the rolling regime, the rotation rate of the particle declined to 21.1 rpm owing to the smaller temperature gradient at the

https://doi.org/10.1021/acsnano.2c03111
ACS Nano 2022, 16, 10878−10889

farther region away from the beam spot. The translation velocity was 2.2 μm/s, whose magnitude was mainly determined by the F_{TE}. Light-powered propulsion can also be realized in our platform as the micro/nanoobject is at least 1.5 body-length away from the laser spot. Figure 3e (also see Supplementary Movie 5) displays the shooting process of a PS microparticle: the particle locomoted at an average velocity of 0.37 μm/s and was powered by a 0.3 mW/μm^2 laser beam with an initial D of 10 μm. We should note that the minimum D for shooting mode was observed as 4.8 μm, which is also close to our theoretical prediction in Figure 2. Different from the translational manipulation in our tweezing mode and other optical tweezers, shooting mode has the advantage of a long working range to effectively manipulate objects in a phototoxicity-free manner. The ionic strength also plays an important role in multimodal manipulation. The TE field, zeta potentials of particles, and surface zeta potentials of the substrate can be affected by the PBS concentration in the solutions. As a result, the rotation rate and translation velocity of a rolling particle increase and then decrease as PBS concentration increases from 0% to 15% (see Supplementary Figure 15). As c(PBS) decreased from 5% to 2.5% then to 0%, the shooting velocity decreases from 0.37 μm/s to 0.28 μm/s and then to zero, because of the decreasing F_{TE}.[45]

Programmable Multimodal Control. To precisely control the laser-particle distance and compensate for the inherent thermal fluctuations of suspended objects (especially for nanoparticles), we integrated feedback control based on real-time imaging into our system (Figure 4a) for active beam-steering, making our platform more efficient, precise, and programmable. Laser beam(s) with arbitrary shapes, sizes, and optical intensities can be instantaneously projected to any position(s) by the spatial light modulator (SLM) for tailorable temperature fields and particle-laser distances. In this way, we can not only automatically switch among different working modes but also precisely adjust the manipulation parameters (e.g., translation velocity) of each mode. The feedback control algorithm is based on the synergy of real-time particle detection and corresponding beam steering via the SLM. Briefly, the real-time position of colloidal particles was tracked and sent to the computer as the input signal; then the output signal (s) was assigned to the SLM or/and motorized stage to project the modulated laser beam toward the calculated positions.

With the automated feedback control, our platform allows to pattern arbitrary shapes using colloidal matter as building blocks. As a demonstration, we succeeded in transforming a "trapezoid" consisted of four microparticles (2 μm) into a "rhombus" with the side length of 7.5 μm in tweezing mode and then enlarging the "rhombus" by 50% through the shooting mode by illuminating its center with a laser beam, which simultaneously shot out the four particles (see Figure 4b and Supplementary Movie 6). Such an automatic colloidal patterning offers an opportunity for dynamic lithography at single-particle resolution. It should be noted that the feedback control accuracy is mainly related to the frame rate of real-time imaging and the refresh time of the motorized stage or SLM, which finally determines the accuracy of D.

Particle manipulation at nanoscale accuracy has been achieved by the SLM-based feedback control. A 200 nm gold nanosphere was chosen as a representative target to validate the precision of our system because its inherent high rotational Brownian motion makes manual control almost impossible. Figure 4c (also see Supplementary Movie 7) displays the trajectory of the nanoparticle actuated by a SLM-modulated single beam. Note that dark-field optical imaging was used for the more accurate monitoring of the gold nanosphere based on its strong light scattering. "UT AUSTIN" was "written" in the dark-field image by automatically rolling the nanosphere with feedback control along the predesigned path. Moreover, the Brownian motion of the nanosphere was significantly suppressed by the real-time feedback control. Specifically, the position of the laser beam was updated according to the real-time imaging, which was calculated based on the consideration of the predesigned path and the compensation of random Brownian motion. Although some motion fluctuations were still observed, the directed swimming reached a high spatial precision compared to the most advanced nanoswimmers and even microswimmers with 1−2 order of magnitude larger sizes (that exhibit 3−10 times smaller Brownian motions) driven by optical,[64] electric,[9] acoustic,[65] and magnetic fields.[66]

Our platform can even work in complex environments where targets are surrounded by nontarget particles as depicted in the inset of Figure 4a. In the current system, the size and brightness of particles are used to differentiate targets from other particles. To validate this capability, a few 2.8 μm PS particles with the attachment fluorescent nanobeads were immersed in the solution containing a large amount of the same PS particles without any nanobead. As shown in Supplementary Movie 8, the target particle, i.e., the PS particle with nanobeads, was recognized immediately and automatically rolled along the predesigned path, while the nontarget particles were ignored by the system. The platform is also capable of the multimodal manipulation of low-dimension nanomaterials such as semiconductor nanowires (Supplementary Movie 9).

***In Situ* Three-Dimensional Single-Cell Characterizations.** Besides the versatile control of synthesized particles, our platform stands out for *in situ* three-dimensional single-cell characterizations based on its remote on-demand multimodal manipulation of individual live cells using light. As an initial demonstration, we have applied our platform to reveal the three-dimensional adhesion characteristics of individual cell surfaces. With various proteins, carbohydrates, and phospholipids, cell surfaces mediate cell−cell and cell-environment communications, playing crucial roles in a variety of cellular events. For instance, the first step of inflammatory response is the rolling adhesion (i.e., rolling followed by adhesion) of hematopoietic cells on vascular surfaces at infected or injured sites.[67] Fungi and bacteria infect a host by rolling near endothelium and then attaching to the epithelial cells through the adhesion force between the cell surfaces.[68] Most of the existing single-cell assays can precisely measure the cellular adhesion dominated by tensile forces.[69,70] However, they are not able to capture the shear kinetics of the rolling cells. With the capability of versatile control of both translational and rotational motions at nanometer resolution, our multimodal micro/nanomanipulation platform provides an effective approach to filling this gap.

To achieve the *in situ* single-cell surface characterization, we manipulated two live yeast cells (*Saccharomyces cerevisiae*) and evaluated the intercellular rotational adhesion at the specific sites. We selected a yeast cell with a uniform surface as a probe and a larger yeast cell with one scar bud (a mark deposited on the surface of a mother cell after cell division) as a target. As shown in Figure 5 (also see Supplementary Movie 10),

https://doi.org/10.1021/acsnano.2c03111
ACS Nano 2022, 16, 10878−10889

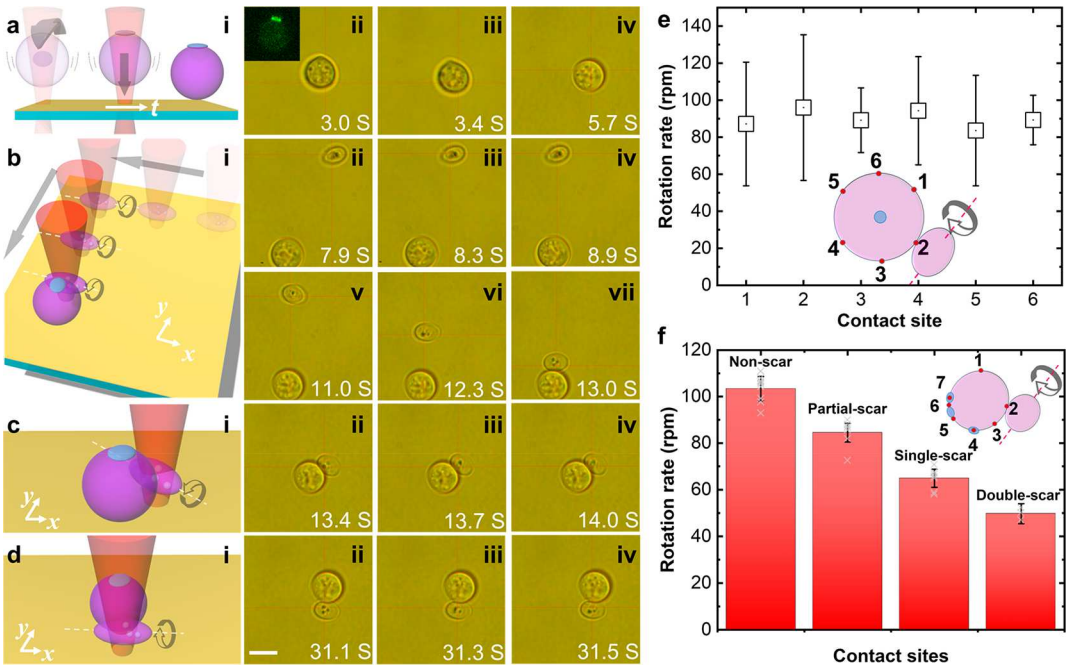

Figure 5. Multimodal manipulation of cells for *in situ* three-dimensional surface characterization at subcellular resolution. (a) Schematic and time-resolved optical images demonstrating the rotation and printing of the target yeast cell (the white arrow is a time axis). Once printed onto the substrate, the cell did not move. Inset of (ii): the fluorescent image of the target yeast cell captured at this moment showing the position of the bud scar region (i.e., bright green region). (b) Schematic (i) and successive optical images (ii−vii) showing the tweezing and rolling of the probe yeast cell, which enables the probe cell to approach the target efficiently. (c and d) Schematics (i) and successive optical images (ii−iv) of the rotation of the probe cell contacting the target cell at the different sites, which enable us to capture the shear kinetics of the cell adhesion dominated by hydrophobic interactions. The linear and curve arrows in the schematics of (a−d) indicate translational and rotational motions. Scale bar: 10 μm. (e) Measured rotation rates of the probe cell contacting the target cell at the six sites in nonscar regions (marked by the red dots in the inset schematic). The scar region was rotated to the top as marked by the blue region in the inset schematic. (f) Measured rotation rates of probe cells contacting target cells at sites in nonscar and bud scar regions. Inset: an illustrative schematic of the three-dimensional cell surface characterization at subcellular resolution. Blue regions - bud scars; red dots - contact sites. The dashed line and curved arrow indicate the rotational direction of the probe cell. Numbers 1−3 are nonscar contact sites; no. 5 is a partial-scar site; nos. 4 and 7 are single-scar sites; no. 6 is a double-scar site. The rotation rates were obtained from four pairs of yeast cells (see Supplementary Figure 17).

initially, the target cell was rotated and printed on the substrate with the bud scar region facing upward to achieve the cell characterization without Brownian motion (Figure 5a). Next, the probe cell was trapped and brought into contact with the target cell through translation and rolling (Figure 5b). Last, the shear kinetics of site-specific intercellular adhesion was quantified by the rotation rate of the probe cell in contact with the target cell at different sites (Figure 5c,d). When the probe cell approaches the target cell at the bud scar region, the rich α-chitin molecules on the probe cell induce strong hydrophobic interactions[71] between the target and probe cells, which generates a depletion region and leads to a hydrophobic bonding force ranging from 1 to 10 pN.[72] For the nonscar regions, the hydrophobic bonding between the oligosaccharides is weaker. Like the rolling adhesion process of hematopoietic cells, the rotation of the probe cell continuously breaks the hydrophobic bonding. When the probe cell approaches the target cell in the scar regions, the stronger hydrophobic bonding between the rich hydrophobic α-chitin molecules in the bud scar region of the target cell and the less-hydrophobic oligosaccharides in the nonscar region of the probe cell slows down the rotation rate of the probe cell. Figure 5e shows the measured rotation rates of the probe cell in contact with the target cell at six different sites (as shown in the inset). As expected, no obvious variation in the rotation rates was observed due to the similar hydrophobicity of the nonscar regions that contacted the probe cell.

To further assess the accuracy and sensitivity of our multimodal platform in the cell surface characterization, we chose an elder yeast cell with multiple bud scars as the target cell. The insets in Figure 5f show the schematic (bottom left) and fluorescence image (top right) indicating the sites of the bud scars (schematic: blue regions; fluorescence image: green regions) on the target cell. A probe cell without bud scars was transported to contact the target cell. The rolling interactions between the probe and target cells in the nonscar region and the scar region were characterized by recording the rotation rates of the probe cells (Figure 5f and also see Supplementary Movie 11). A rotation rate of ∼103.4 rpm was obtained at nonscar locations, while a rotation rate (64.9 rpm) of the probe cells in full contact with the scar regions is much smaller. The decreased rotation rate results from the increased adhesion between the probe and target cells in the presence of the scar. Notably, our platform is sensitive enough to detect the adhesion difference at the subscar-region level. When the probe cell partially contacted the bud scar region, an intermediate rotation rate (84.5 rpm) was measured. When the probe cell simultaneously contacted two scar regions, a minimum rotation rate (49.7 rpm) was observed, suggesting the strongest adhesion. In the cell experiments, a weakly focused laser beam [numerical aperture (NA) = 0.5−0.7] with

https://doi.org/10.1021/acsnano.2c03111
ACS Nano 2022, 16, 10878−10889

low intensity (0.06 mW/μm^2) was used to provide a small temperature rise (<9 K). With the capability of manipulating and measuring human cells (see Supplementary Movies 12 and 13 and Supplementary Figure 16) with subcellular resolution, this *in situ* three-dimensional cellular surface characterization technique is promising for gaining insights into cell−cell communication for biological study, tissue engineering, immunotherapy, and drug development.[73]

CONCLUSIONS

Through coordination of light, heat, and mass transfer at liquid/solid interfaces, we have achieved a versatile micro/nanomanipulation platform that allows multimodal translation and rotation of synthetic particles and live cells at single-particle resolution with simple optics. Tweezing, printing, rotating, rolling, and shooting of particles and cells have been achieved in the same system and can be switched on demand by simply controlling the laser-particle distance or optical power. Automatic operation of the micro/nanoparticles with high precision at the nanoscale is demonstrated with a SLM and a customized algorithm for feedback control. In principle, our platform is applicable to manipulating arbitrary micro/nanoscale objects of diverse compositions, sizes, and shapes through proper surface modification of the objects. As a proof-of-concept, *in situ* three-dimensional cell surface characterizations at the subcell level have been achieved by multimodal cell manipulation.

We believe that our versatile platform will serve as a powerful toolbox for applications in colloidal science, cell biology, nanomaterials, and micro/nanorobotics, either functioning in one single mode or operating in multiple modes. For instance, using the rotating (or rolling) of isotropic objects reported here, one can shed light on the rolling adhesion of cells and bacteria at the single-cell level. By combining rotating and printing modes, we can expose certain spots of the particles with heterogeneous surface properties to the illuminating light source for spot-specific optical characterizations. Through synergizing three or more operation modes, one can carry out more sophisticated studies of the cell−cell or cell-particle interactions, as demonstrated in the subcellular surface characterizations. For fragile objects, shooting mode with the lower optical power can be applied instead of tweezing to minimize the optical or optothermal damage. The multimodal optothermal manipulation platform is also promising for constructing functional micro/nano-architected materials with colloidal particles as building blocks.[74,75] In addition, our platform is expected to facilitate the development of super-resolution imaging techniques. For example, total internal reflection fluorescence microscopy (TIRFM) has improved the detection limit to <100 nm through evanescent waves generated at solid/liquid interfaces.[76] However, it is challenging for TIRFM to fully analyze a micro-object in three dimensions due to the exponential decay of evanescent waves. Three-dimensional TIRFM imaging of cells can be achieved by pulling, rotating, and printing target cells with a large-NA (NA > 1.49) objective and additional mirrors for a large angle of incidence in our platform, which would make it applicable to heterogeneous biological samples.

Because of the use of a light-absorbing substrate, we expect that the platform would play an important role in *in vitro* biological study. The multimodal manipulation of cells in native biofluids (e.g., plasma) is feasible as long as the biofluids contain ions and biomolecules for the formation of electric and osmotic fields. Optothermal substrates with high near-infrared (NIR) optothermal conversion efficiencies such as hyper-branched Au plasmonic substrate[77] can be applied to extend the working wavelength of our platform to the NIR regime. By exploiting surface chemistry to modify the optothermal substrates to be either positively or negatively charged, one can apply the platform to manipulate synthetic particles and live cells of any type of surface charge.

METHODS

Microscopy Setup. A sketch of the experimental setup is shown in Figure 4. A 660 nm laser beam (Laser Quantum, Opus 660) was expanded with a 5× beam expander (Thorlabs, GBE05-A) and directed to a Nikon inverted microscope (Nikon, Ti-E) with a 100× oil objective (Nikon, CFI Plan Fluor 100XS Oil) for the manipulation experiments inside a microfluidic chamber of ∼120 μm thickness. A Nikon upright microscope (Nikon, Eclipse Ni) with 40× air objective (Nikon, CFI Plan Fluor 40X) was used for automated manipulation experiments. For the dark-field optical imaging, an air condenser (Nikon, C-AA Achromat/Aplanat Condenser) was used to focus the incident white light onto the sample from the top. A complementary metal-oxide-semiconductor (CMOS) camera (Nikon, DS-Fi3) or a charge-coupled device (CCD) camera (Lumenera, 12 fps) was used to record the optical images. A Notch filter (658 nm) was placed between the objective and camera to block the incident laser beam. White light was directed from the top (bottom for the upright microscope) of the stage for bright-field imaging. A xenon lamp (Sutter Instrument Lambda, LB-LS/30) was applied through the objective with a GFP filter cube (457−487/502−538 nm for excitation/emission) for fluorescence imaging. The notch filter was removed in fluorescence imaging. The dichroic beam splitter was selected according to the excitation, emission, and laser wavelength.

Sample Preparation. A 15 μL PEG/PBS solution with particles or cells was added on a plasmonic substrate with a spacer (Secure-Seal), and then an upper coverslip (Thermo Fisher Scientific, 18 × 18 mm^2) was placed on top, generating a ∼120 μm liquid film between the glass coverslips. The plasmonic substrates were fabricated by a three-step process: 5.5 nm Au films were thermally deposited on glass slides (Thermo Fisher Scientific, 22 × 22 mm^2) at a base pressure of 8 × 10^{-6} Torr. Then the Au films were annealed at 550 °C for 2 h. Finally, the substrates were immersed in PBS solution with 1% BSA (Sigma-Aldrich, A8531) at room temperature for 24 h, followed by rinsing with deionized (DI) water (Milli-Q) and drying under a nitrogen stream. 5−15 wt % PEG 20000 powder (Sigma-Aldrich, 8.18897) and 1% particle/cell solution were dissolved in diluted PBS solution (Sigma-Aldrich, 806552) to obtain the targeted PEG/PBS solution. Ultrasonic Bath (Branson, CPX5800H) was used to disperse the particles uniformly. Then 1 wt % 2.8 μm PS beads with carboxylic functional groups and streptavidin ligands on the surface (Thermo Fisher Scientific, 65306) were diluted with 5% PBS solution by 1000 times, followed by adding 1‰ 40 nm yellow-green fluorescent (505/515), biotin-labeled nanobeads solution (Thermo Fisher Scientific, F8766). Then the mixed solution was stored at 4 °C for 12 h followed by centrifugation at 8000 rpm for 5 min at room temperature. Yeast cells (Red Star) were washed three times and resuspended in DI to obtain a cell density of ∼5E5 cells/mL. Then 200 nm gold nanospheres or 2 μm PS beads (Bangs Laboratories) were diluted with PBS/PEG solution by 1000 times for automated manipulation experiments.

Feedback Control. Achieved by LabVIEW programs (LabVIEW 18.0, National Instruments), the feedback control for automated manipulation of the optothermal micro/nanoparticles was based on adaptive laser steering fed by real-time particle tracking. The geometric information, preferred working mode, and designed path of the target particles were preset before the program ran. Once the program was started, all the manipulation would be achieved automatically. Specifically, the images were first captured by a CCD camera (Lumenera, 12 fps) with 1392 × 1040 pixels. The target particles were detected by transforming the captured images into

https://doi.org/10.1021/acsnano.2c03111
ACS Nano 2022, 16, 10878−10889

binary ones and applying certain thresholds (shape, area, etc.) via the IMAQ particle filter module in LabVIEW to recognize the target objects. The pixel coordinates of the target particles' geometrical centers were then obtained by the IMAQ particle analysis module. Afterward, the laser(s) were automatically positioned at a certain distance D away from the target objects in terms of the predesigned working modes and in a certain direction according to the preset moving path. The laser could be steered either by the motorized stage (PRIOR, H101A/D) or the SLM (HAMAMATSU, X13138). As for the motorized-stage type, the stage was controlled by our home-built LabVIEW program, which changed the sample's position relative to the laser beam. The laser beam could always maintain good quality as no phase modulation was applied to it. However, it could not be split into multiple beams for high-throughput manipulation, and it was not suitable for the "rolling" mode due to the relatively high intervals between two movements of the stage. As for the SLM type, we modified a custom-written LabVIEW interface called *Red Tweezers*.[78] The laser beam was placed at the predesigned positions without frequent stage motion if the target particle did not move out of the original imaging scope. This method permitted multibeam steering and could respond very quickly but would introduce unwanted diffracted light over the manipulation region. All in all, the aforementioned imaging capturing, imaging processing, and laser steering were carried out in sequence for every frame of the camera, which enabled real-time and automated manipulation of the optothermal micronanorobots.

Numerical Simulations. FEA simulations: COMSOL Multiphysics (ver. 5.4a) was used in FEA simulations to calculate the temperature distribution and electrical potential. Laser heating was modeled as heat influx with a Gaussian beam profile with laser power, beam width, and absorptivity as the inputs to define the heating source at the bottom edge of the simulation domain. A particle on a substrate was introduced, with varying positions from the laser beam axis. The temperatures on the substrate and the particle surface were obtained as a discrete data set from COMSOL. The depletion, thermoelectric, and electrokinetic force were evaluated in MATLAB (ver 2020). Modeling details are shown in Supplementary Note 2 including the modeling framework, governing equations, and boundary conditions.

FDTD simulation: Lumerical was used in finite-difference time-domain simulations to calculate optical forces and torques. The refractive indices of the PS particles, glass substrate, and the solution were set as 1.58, 1.52, and 1.34,[79] respectively. To model the plasmonic substrate (AuNIs), a SEM image of the substrate (Supplementary Figure 4) was imported into the model. We scaled the image appropriately for accurate modeling of nanoparticle sizes and spacings. The permittivity of the Au films was taken from Johnson and Christy.[80] The optical forces and torques were calculated through the Maxwell stress tensor (MST) at an excitation wavelength of 660 nm. A Gaussian laser beam was used as the excitation source and launched from the glass substrate side. The boundary conditions for all directions were set as perfectly matched layers. The mesh size in the simulation was set as 5 nm.

Temperature Measurements. Temperature distributions were obtained through thermal imaging with quadriwave shearing interferometry (TIQSI).[81] A thermal imaging camera (SID4-HR, Phasics) was coupled to the inverted microscope with a × 100 oil objective. Thermal images were recorded using SIDFTHERMO software (Phasics). Note that we utilized DI water as a medium for temperature measurements because the refractive index of the PEG/PBS solution in the software is not available. The measurements are still valid because there is a small difference between the thermal conductivity of the PEG/PBS solution and that of water. The thermal conductivity of a PEG solution can be calculated by[82]

$$\lambda_{\mathrm{PEGsolution}} = \left(\frac{\lambda_{\mathrm{PEG}}}{\lambda_{\mathrm{EG}}}\right)^{*} x + \lambda_{\mathrm{water}}{}^{*}(1 - x)$$

where x is the weight percentage of PEG 20000 in PEG solution and λ_{PEG}, λ_{EG}, and λ_{water} are the thermal conductivity of PEG, ethylene glycol, and water, respectively. Substituting the thermal conductivity data[83,84] and weight percentages of PEG (5%−15%), we obtained $\lambda_{\mathrm{PEG\ solution}}$, 0.56−0.59 W/m·K, which is very close to the value of water, 0.6 W/m·K.

Dynamic Light Scattering Measurements. Dynamic light scattering (DLS) measurements were performed using Malvern Zetasizer Nano ZS equipped in a backscattering configuration. For the zeta potential of particles, samples were loaded into a prerinsed folded capillary cell and measured at 25−65 °C at an applied voltage of 150 V. Measurements of the surface zeta potential of the light-absorbing substrates: first, cut large substrates into rectangular pieces of 6 mm × 4 mm using a dicing saw (Disco 321 Wafer Dicing Saw) and loaded the surface zeta potential cell with one piece of the substrate. Then, inserted the cell (MS ZEN3600, Malvern Panalytical) into the target PEG/PBS solutions containing tracer particles (300 nm PS particles) and measured the potentials at six positions with distances of 125, 250, 375, 500, 625, and 1000 μm away from the substrate (Supplementary Figure 5a). For distances between 125 and 625 μm, the mobility of tracker particles was controlled by electro-osmotic and electrophoretic force. The zeta potential of the tracker particles was measured at a distance of 1000 μm where an electrophoresis-dominated motion happened. The surface zeta potential is given by $\zeta_{\mathrm{surface}} = -\mathrm{intercept} + \zeta_{\mathrm{tracker}}$, where the intercept is calculated from the first four measurements and ζ_{tracker} is the zeta potential of the tracker particle. The dependence of the surface zeta potential of AuNIs with BSA coating on temperature was investigated.

ASSOCIATED CONTENT

Supporting Information

The Supporting Information is available free of charge at https://pubs.acs.org/doi/10.1021/acsnano.2c03111.

Tweezing mode: trapping and manipulation of a 2.8 μm PS particle (fluorescent microscopy) (MP4)
Printing mode: printing process of a 2.8 μm PS particle (fluorescent microscopy, 2× original speed) (MP4)
Rotating mode: rotation of a 2.8 μm PS particle (fluorescent microscopy) (MP4)
Rolling mode: combined rotation and translation of a 2.8 μm PS particle (fluorescent microscopy) (MP4)
Shooting mode: shooting a 2.8 μm PS particle (fluorescent microscopy) (MP4)
Dynamic patterning using four 2 μm PS particles (2× original speed) (MP4)
Automated feedback swimming of a 200 nm gold nanosphere (dark-field imaging, 5× original speed) (MP4)
Automatic rolling of a selected 2.8 μm PS particle in a complex environment (fluorescent microscopy, one-half original speed) (MP4)
Shooting and rotating of a 5 μm silicon nanowire (original speed) (MP4)
Multimodal manipulation of yeast cells and adhesion characterization of a uniform cell surface (2× original speed) (MP4)
Adhesion characterization of a nonuniform cell surface (2× original speed) (MP4)
Rotation of a red blood cell in the cell culture media (RPMI-1640, 10%FBS, and 1% 5000U/ml penicillin-streptomycin) with 2% PEG (original speed) (MP4)
Rotation of a white blood cell (NJ76) in the cell culture media (RPMI-1640, 10% FBS, and 1% 5000U/ml penicillin-streptomycin) with 2% PEG (original speed) (MP4)
Simulations of the formation of TE field and the laser-generated temperature field, calculation of optical forces,

https://doi.org/10.1021/acsnano.2c03111
ACS Nano 2022, 16, 10878−10889

scanning electron micrographs of AuNIs substrates, measurement of zeta potentials and surface zeta potentials, multiphysics models on temperature and solute concentration, light-powered thermal forces, measurement of the temperature fields (PDF)

AUTHOR INFORMATION

Corresponding Author

Yuebing Zheng − *Walker Department of Mechanical Engineering, The University of Texas at Austin, Austin, Texas 78712, United States; Materials Science & Engineering Program and Texas Materials Institute and Department of Electrical and Computer Engineering, The University of Texas at Austin, Austin, Texas 78712, United States;* orcid.org/0000-0002-9168-9477; Email: zheng@austin.utexas.edu

Authors

Hongru Ding − *Walker Department of Mechanical Engineering, The University of Texas at Austin, Austin, Texas 78712, United States;* orcid.org/0000-0003-1579-6825

Zhihan Chen − *Materials Science & Engineering Program and Texas Materials Institute, The University of Texas at Austin, Austin, Texas 78712, United States*

Pavana Siddhartha Kollipara − *Walker Department of Mechanical Engineering, The University of Texas at Austin, Austin, Texas 78712, United States;* orcid.org/0000-0003-0166-6720

Yaoran Liu − *Department of Electrical and Computer Engineering, The University of Texas at Austin, Austin, Texas 78712, United States*

Youngsun Kim − *Materials Science & Engineering Program and Texas Materials Institute, The University of Texas at Austin, Austin, Texas 78712, United States;* orcid.org/0000-0001-5219-8408

Suichu Huang − *Walker Department of Mechanical Engineering, The University of Texas at Austin, Austin, Texas 78712, United States; Materials Science & Engineering Program and Texas Materials Institute, The University of Texas at Austin, Austin, Texas 78712, United States; Key Laboratory of Micro-Systems and Micro-Structures Manufacturing of Ministry of Education and School of Mechatronics Engineering, Harbin Institute of Technology, Harbin 15001, China;* orcid.org/0000-0001-5057-8095

Complete contact information is available at: https://pubs.acs.org/10.1021/acsnano.2c03111

Author Contributions

H.D. and Y.Z. conceived the idea for this study. H.D. prepared materials and worked on the experiments. Z.C. designed the automated control system and collected the related data with H.D. P.K. and H.D. conducted the simulations. H.D. and Y.K. fabricated the substrates. H.D., Y.L., and S.H. built the optical setup. Y.Z. supervised the project. H.D. and Y.Z. wrote the manuscript with the inputs of all other authors.

Notes

The authors declare no competing financial interest.

ACKNOWLEDGMENTS

H.D., Z.C., P.S.K., Y.L., Y.K., S.H., and Y.Z. acknowledge financial support from the National Science Foundation (NSF-ECCS-2001650), the National Aeronautics and Space Administration (80NSSC17K0520), and the National Institute of General Medical Sciences of the National Institutes of Health (DP2GM128446). We thank the Texas Advanced Computing Centre (TACC) at The University of Texas at Austin for providing HPC resources that contributed to the research results reported within this paper. URL: http://www.tacc.utexas.edu. We also thank Dr. Kan Yao, Dr. Xiaolei Peng, and Dr. Jingang Li for their assistance in experiments.

REFERENCES

(1) Medina-Sanchez, M.; Schmidt, O. G. Medical Microbots Need Better Imaging and Control. *Nature* **2017**, *545*, 406−408.

(2) Douglas, S. M.; Bachelet, I.; Church, G. M. A Logic-Gated Nanorobot for Targeted Transport of Molecular Payloads. *Science* **2012**, *335*, 831−834.

(3) Pauzauskie, P. J.; Radenovic, A.; Trepagnier, E.; Shroff, H.; Yang, P.; Liphardt, J. Optical Trapping and Integration of Semiconductor Nanowire Assemblies in Water. *Nat. Mater.* **2006**, *5*, 97−101.

(4) Marago, O. M.; Jones, P. H.; Gucciardi, P. G.; Volpe, G.; Ferrari, A. C. Optical Trapping and Manipulation of Nanostructures. *Nat. Nanotechnol.* **2013**, *8*, 807−19.

(5) Qian, B.; Montiel, D.; Bregulla, A.; Cichos, F.; Yang, H. Harnessing Thermal Fluctuations for Purposeful Activities: The Manipulation of Single Micro-Swimmers by Adaptive Photon Nudging. *Chem. Sci.* **2013**, *4*, 1420−1429.

(6) Tian, Z.; Yang, S.; Huang, P. H.; Wang, Z.; Zhang, P.; Gu, Y.; Bachman, H.; Chen, C.; Wu, M.; Xie, Y.; Huang, T. J. Wave Number-Spiral Acoustic Tweezers for Dynamic and Reconfigurable Manipulation of Particles and Cells. *Sci. Adv.* **2019**, *5*, No. eaau6062.

(7) Jeon, S.; Kim, S.; Ha, S.; Lee, S.; Kim, E.; Kim, S. Y.; Park, S. H.; Jeon, J. H.; Kim, S. W.; Moon, C.; Nelson, B. J.; Kim, J.-y.; Yu, S.-W.; Choi, H. Magnetically Actuated Microrobots as a Platform for Stem Cell Transplantation. *Sci. Robot.* **2019**, *4*, No. eaav4317.

(8) Chen, C.; Tang, S.; Teymourian, H.; Karshalev, E.; Zhang, F.; Li, J.; Mou, F.; Liang, Y.; Guan, J.; Wang, J. Chemical/Light-Powered Hybrid Micromotors with "on-the-Fly" Optical Brakes. *Angew. Chem., Int. Ed. Engl.* **2018**, *57*, 8110−8114.

(9) Mano, T.; Delfau, J. B.; Iwasawa, J.; Sano, M. Optimal Run-and-Tumble-Based Transportation of a Janus Particle with Active Steering. *Proc. Natl. Acad. Sci. U. S. A.* **2017**, *114*, E2580−E2589.

(10) Ashkin, A. Acceleration and Trapping of Particles by Radiation Pressure. *Phys. Rev. Lett.* **1970**, *24*, 156−159.

(11) Xu, L.; Mou, F.; Gong, H.; Luo, M.; Guan, J. Light-Driven Micro/Nanomotors: From Fundamentals to Applications. *Chem. Soc. Rev.* **2017**, *46*, 6905−6926.

(12) Ghosh, S.; Ghosh, A. Mobile Nanotweezers for Active Colloidal Manipulation. *Sci. Robot.* **2018**, *3*, eaaq0076.

(13) Yan, Z.; Sajjan, M.; Scherer, N. F. Fabrication of a Material Assembly of Silver Nanoparticles Using the Phase Gradients of Optical Tweezers. *Phys. Rev. Lett.* **2015**, *114*, 143901.

(14) Lin, L.; Wang, M.; Peng, X.; Lissek, E. N.; Mao, Z.; Scarabelli, L.; Adkins, E.; Coskun, S.; Unalan, H. E.; Korgel, B. A.; Liz-Marzan, L. M.; Florin, E. L.; Zheng, Y. Opto-Thermoelectric Nanotweezers. *Nat. Photonics* **2018**, *12*, 195−201.

(15) Alam, M. S.; Zhan, Q.; Zhao, C. Additive Opto-Thermomechanical Nanoprinting and Nanorepairing under Ambient Conditions. *Nano Lett.* **2020**, *20*, 5057−5064.

(16) Zhao, C.; Shah, P. J.; Bissell, L. J. Laser Additive Nano-Manufacturing under Ambient Conditions. *Nanoscale* **2019**, *11*, 16187−16199.

(17) Chen, C.; Mou, F.; Xu, L.; Wang, S.; Guan, J.; Feng, Z.; Wang, Q.; Kong, L.; Li, W.; Wang, J.; Zhang, Q. Light-Steered Isotropic Semiconductor Micromotors. *Adv. Mater.* **2017**, *29*, 1603374.

(18) Khadka, U.; Holubec, V.; Yang, H.; Cichos, F. Active Particles Bound by Information Flows. *Nat. Commun.* **2018**, *9*, 3864.

(19) Lee, E.; Luo, T. Long-Distance Optical Pulling of Nanoparticle in a Low Index Cavity Using a Single Plane Wave. *Sci. Adv.* **2020**, *6*, No. eaaz3646.

(20) Lin, L.; Kollipara, P. S.; Kotnala, A.; Jiang, T.; Liu, Y.; Peng, X.; Korgel, B. A.; Zheng, Y. Opto-Thermoelectric Pulling of Light-Absorbing Particles. *Light Sci. Appl.* **2020**, *9*, 34.
(21) Liu, M.; Zentgraf, T.; Liu, Y.; Bartal, G.; Zhang, X. Light-Driven Nanoscale Plasmonic Motors. *Nat. Nanotechnol.* **2010**, *5*, 570−3.
(22) Han, F.; Parker, J. A.; Yifat, Y.; Peterson, C.; Gray, S. K.; Scherer, N. F.; Yan, Z. Crossover from Positive to Negative Optical Torque in Mesoscale Optical Matter. *Nat. Commun.* **2018**, *9*, 4897.
(23) Liang, Z.; Fan, D. Visible Light-Gated Reconfigurable Rotary Actuation of Electric Nanomotors. *Sci. Adv.* **2018**, *4*, No. eaau0981.
(24) Ding, H.; Chen, Z.; Zheng, Y. *Versatile Optothermal Micro/Nanorobots for Cellular Biology*; Proc.SPIE, 2020.
(25) Lee, E.; Huang, D.; Luo, T. Ballistic Supercavitating Nanoparticles Driven by Single Gaussian Beam Optical Pushing and Pulling Forces. *Nat. Commun.* **2020**, *11*, 2404.
(26) Andren, D.; Baranov, D. G.; Jones, S.; Volpe, G.; Verre, R.; Kall, M., Microscopic Metavehicles Powered and Steered by Embedded Optical Metasurfaces. *Nat. Nanotechnol.* **2021**.*16*970
(27) Shao, L.; Käll, M. Light-Driven Rotation of Plasmonic Nanomotors. *Adv. Funct. Mater.* **2018**, *28*, 1706272.
(28) Tong, L.; Miljkovic, V. D.; Kall, M. Alignment, Rotation, and Spinning of Single Plasmonic Nanoparticles and Nanowires Using Polarization Dependent Optical Forces. *Nano Lett.* **2010**, *10*, 268−73.
(29) Shao, L.; Yang, Z. J.; Andren, D.; Johansson, P.; Kall, M. Gold Nanorod Rotary Motors Driven by Resonant Light Scattering. *ACS Nano* **2015**, *9*, 12542−51.
(30) Reimann, R.; Doderer, M.; Hebestreit, E.; Diehl, R.; Frimmer, M.; Windey, D.; Tebbenjohanns, F.; Novotny, L. Ghz Rotation of an Optically Trapped Nanoparticle in Vacuum. *Phys. Rev. Lett.* **2018**, *121*, 033602.
(31) Schmidt, F.; Magazzu, A.; Callegari, A.; Biancofiore, L.; Cichos, F.; Volpe, G. Microscopic Engine Powered by Critical Demixing. *Phys. Rev. Lett.* **2018**, *120*, 068004.
(32) Hansen, P. M.; Bhatia, V. K.; Harrit, N.; Oddershede, L. Expanding the Optical Trapping Range of Gold Nanoparticles. *Nano Lett.* **2005**, *5*, 1937−42.
(33) Babynina, A.; Fedoruk, M.; Kuhler, P.; Meledin, A.; Doblinger, M.; Lohmuller, T. Bending Gold Nanorods with Light. *Nano Lett.* **2016**, *16*, 6485−6490.
(34) Rasmussen, M. B.; Oddershede, L. B.; Siegumfeldt, H. Optical Tweezers Cause Physiological Damage to Escherichia Coli and Listeria Bacteria. *Appl. Environ. Microbiol.* **2008**, *74*, 2441−6.
(35) Maier, C. M.; Huergo, M. A.; Milosevic, S.; Pernpeintner, C.; Li, M.; Singh, D. P.; Walker, D.; Fischer, P.; Feldmann, J.; Lohmuller, T. Optical and Thermophoretic Control of Janus Nanopen Injection into Living Cells. *Nano Lett.* **2018**, *18*, 7935−7941.
(36) Peng, X.; Chen, Z.; Kollipara, P. S.; Liu, Y.; Fang, J.; Lin, L.; Zheng, Y. Opto-Thermoelectric Microswimmers. *Light Sci. Appl.* **2020**, *9*, 141.
(37) Wang, C.; Chowdhury, S.; Gupta, S. K.; Losert, W. Optical Micromanipulation of Active Cells with Minimal Perturbations: Direct and Indirect Pushing. *J. Biomed. Opt.* **2013**, *18*, 045001.
(38) Dai, B.; Wang, J.; Xiong, Z.; Zhan, X.; Dai, W.; Li, C. C.; Feng, S. P.; Tang, J. Programmable Artificial Phototactic Microswimmer. *Nat. Nanotechnol.* **2016**, *11*, 1087−1092.
(39) Grigorenko, A. N.; Roberts, N. W.; Dickinson, M. R.; Zhang, Y. Nanometric Optical Tweezers Based on Nanostructured Substrates. *Nat. Photonics* **2008**, *2*, 365−370.
(40) Butaite, U. G.; Gibson, G. M.; Ho, Y. D.; Taverne, M.; Taylor, J. M.; Phillips, D. B. Indirect Optical Trapping Using Light Driven Micro-Rotors for Reconfigurable Hydrodynamic Manipulation. *Nat. Commun.* **2019**, *10*, 1215.
(41) Ding, H.; Kollipara, P. S.; Kim, Y.; Kotnala, A.; Li, J.; Chen, Z.; Zheng, Y. Universal Optothermal Micro/Nanoscale Rotors. *Sci. Adv.* **2022**, *8*, No. eabn8498.
(42) Kreysing, M.; Ott, D.; Schmidberger, M. J.; Otto, O.; Schurmann, M.; Martin-Badosa, E.; Whyte, G.; Guck, J. Dynamic Operation of Optical Fibres Beyond the Single-Mode Regime Facilitates the Orientation of Biological Cells. *Nat. Commun.* **2014**, *5*, 5481.
(43) Jiang, H. R.; Wada, H.; Yoshinaga, N.; Sano, M. Manipulation of Colloids by a Nonequilibrium Depletion Force in a Temperature Gradient. *Phys. Rev. Lett.* **2009**, *102*, 208301.
(44) Maeda, Y. T.; Tlusty, T.; Libchaber, A. Effects of Long DNA Folding and Small Rna Stem-Loop in Thermophoresis. *Proc. Natl. Acad. Sci. U. S. A.* **2012**, *109*, 17972−7.
(45) Ding, H.; Kollipara, P. S.; Lin, L.; Zheng, Y. Atomistic Modeling and Rational Design of Optothermal Tweezers for Targeted Applications. *Nano Res.* **2021**, *14*, 295−303.
(46) Chen, Z.; Kollipara, P. S.; Ding, H.; Pughazhendi, A.; Zheng, Y. Liquid Optothermoelectrics: Fundamentals and Applications. *Langmuir* **2021**, *37*, 1315−1336.
(47) Precupas, A.; Leonties, A. R.; Neacsu, A.; Sandu, R.; Popa, V. T. Gallic Acid Influence on Bovine Serum Albumin Thermal Stability. *New J. Chem.* **2019**, *43*, 3891−3898.
(48) Nithiyasri, P.; Balaji, K.; Brindha, P.; Parthasarathy, M. Programmable Self-Assembly of Carbon Nanotubes Assisted by Reversible Denaturation of a Protein. *Nanotechnology* **2012**, *23*, 465603.
(49) Sapir, L.; Harries, D. Is the Depletion Force Entropic? Molecular Crowding Beyond Steric Interactions. *Curr. Opin. Colloid Interface Sci.* **2015**, *20*, 3−10.
(50) Tazhibaeva, S. M.; Musabekov, K. B.; Orazymbetova, A. B.; Zhubanova, A. A. Surface Properties of Yeast Cells. *Colloid J.* **2003**, *65*, 122−124.
(51) van der Wal, A.; Norde, W.; Zehnder, A. J. B.; Lyklema, J. Determination of the Total Charge in the Cell Walls of Gram-Positive Bacteria. *Colloids Surf., B* **1997**, *9*, 81−100.
(52) Buzatu, S. The Temperature-Induced Changes in Membrane Potential. *Riv. Biol.* **2009**, *102*, 199−217.
(53) Blandamer, M. J.; Burgess, J.; Duce, P. P.; Robertson, R. E.; Scott, J. W. M. Analysis of the Dependence on Temperature of the Acid Dissociation Constants for Mono-Carboxylic Acids in Water in Terms of a Two-Stage Mechanism. *J. Chem. Soc., Faraday Trans.1* **1981**, *77*, 2281−2286.
(54) Atkins, P.; de Paula, J. *Physical Chemistry*, 8th ed.; Oxford University Press: New York, 2006; Vol. *7*, pp 211.
(55) Bregulla, A. P.; Wurger, A.; Gunther, K.; Mertig, M.; Cichos, F. Thermo-Osmotic Flow in Thin Films. *Phys. Rev. Lett.* **2016**, *116*, 188303.
(56) Gargiulo, J.; Brick, T.; Violi, I. L.; Herrera, F. C.; Shibanuma, T.; Albella, P.; Requejo, F. G.; Cortes, E.; Maier, S. A.; Stefani, F. D. Understanding and Reducing Photothermal Forces for the Fabrication of Au Nanoparticle Dimers by Optical Printing. *Nano Lett.* **2017**, *17*, 5747−5755.
(57) Heidari, M.; Bregulla, A.; Muinos Landin, S.; Cichos, F.; von Klitzing, R. Self-Propulsion of Janus Particles near a Brush-Functionalized Substrate. *Langmuir* **2020**, *36*, 7775−7780.
(58) Majee, A.; Würger, A. Thermocharge of a Hot Spot in an Electrolyte Solution. *Soft Matter* **2013**, *9*, 2145−2153.
(59) Putnam, S. A.; Cahill, D. G. Transport of Nanoscale Latex Spheres in a Temperature Gradient. *Langmuir* **2005**, *21*, 5317−23.
(60) Wurger, A. Transport in Charged Colloids Driven by Thermoelectricity. *Phys. Rev. Lett.* **2008**, *101*, 108302.
(61) Jia, D.; Hamilton, J.; Zaman, L. M.; Goonewardene, A. The Time, Size, Viscosity, and Temperature Dependence of the Brownian Motion of Polystyrene Microspheres. *Am. J. Phys.* **2007**, *75*, 111−115.
(62) Mo, J.; Simha, A.; Raizen, M. G. Broadband Boundary Effects on Brownian Motion. *Phys. Rev. E Stat. Nonlin. Soft Matter Phys.* **2015**, *92*, 062106.
(63) Huang, L.; Zhao, P.; Liang, F.; Wang, W. Single-Cell 3d Electro-Rotation. *Methods Cell Biol.* **2018**, *148*, 97−116.
(64) Zhan, X.; Zheng, J.; Zhao, Y.; Zhu, B.; Cheng, R.; Wang, J.; Liu, J.; Tang, J.; Tang, J. From Strong Dichroic Nanomotor to Polarotactic Microswimmer. *Adv. Mater.* **2019**, *31*, No. e1903329.
(65) Ding, X.; Lin, S. C.; Kiraly, B.; Yue, H.; Li, S.; Chiang, I. K.; Shi, J.; Benkovic, S. J.; Huang, T. J. On-Chip Manipulation of Single

https://doi.org/10.1021/acsnano.2c03111
ACS Nano 2022, 16, 10878−10889

Microparticles, Cells, and Organisms Using Surface Acoustic Waves. *Proc. Natl. Acad. Sci. U. S. A.* **2012**, *109*, 11105−9.
(66) Zhou, H.; Mayorga-Martinez, C. C.; Pane, S.; Zhang, L.; Pumera, M. Magnetically Driven Micro and Nanorobots. *Chem. Rev.* **2021**, *121*, 4999−5041.
(67) McEver, R. P.; Zhu, C. Rolling Cell Adhesion. *Annu. Rev. Cell Dev. Biol.* **2010**, *26*, 363−96.
(68) Stewart, G., Yeast Flocculation—Sedimentation and Flotation. *Fermentation* **2018**, *4*.28
(69) Huang, J.; Zarnitsyna, V. I.; Liu, B.; Edwards, L. J.; Jiang, N.; Evavold, B. D.; Zhu, C. The Kinetics of Two-Dimensional Tcr and Pmhc Interactions Determine T-Cell Responsiveness. *Nature* **2010**, *464*, 932−6.
(70) Yang, J.; Petitjean, S. J. L.; Koehler, M.; Zhang, Q.; Dumitru, A. C.; Chen, W.; Derclaye, S.; Vincent, S. P.; Soumillion, P.; Alsteens, D. Molecular Interaction and Inhibition of Sars-Cov-2 Binding to the Ace2 Receptor. *Nat. Commun.* **2020**, *11*, 4541.
(71) Holan, Z. k.; Pokorn, V.; Beran, K.; Gemperle, A.; Tuzar, Z. k.; Baldrin, J. The Glucan-Chitin Complex in Saccharomyces Cerevisiae. *Arch. Microbiol.* **1981**, *130*, 312−318.
(72) Castelain, M.; Pignon, F.; Piau, J. M.; Magnin, A.; Mercier-Bonin, M.; Schmitz, P. Removal Forces and Adhesion Properties of Saccharomyces Cerevisiae on Glass Substrates Probed by Optical Tweezer. *J. Chem. Phys.* **2007**, *127*, 135104.
(73) Weber, E. W.; Maus, M. V.; Mackall, C. L. The Emerging Landscape of Immune Cell Therapies. *Cell* **2020**, *181*, 46−62.
(74) Lin, L.; Lepeshov, S.; Krasnok, A.; Jiang, T.; Peng, X.; Korgel, B. A.; Alu, A.; Zheng, Y. All-Optical Reconfigurable Chiral Meta-Molecules. *Mater. Today* **2019**, *25*, 10−20.
(75) Li, J.; Wang, M.; Wu, Z.; Li, H.; Hu, G.; Jiang, T.; Guo, J.; Liu, Y.; Yao, K.; Chen, Z.; Fang, J.; Fan, D.; Korgel, B. A.; Alu, A.; Zheng, Y. Tunable Chiral Optics in All-Solid-Phase Reconfigurable Dielectric Nanostructures. *Nano Lett.* **2021**, *21*, 973−979.
(76) Fish, K. N. Total Internal Reflection Fluorescence (Tirf) Microscopy. *Curr. Protoc Cytom* **2009**, *Chapter 12*, 18.
(77) Zhou, J.; Jiang, Y.; Hou, S.; Upputuri, P. K.; Wu, D.; Li, J.; Wang, P.; Zhen, X.; Pramanik, M.; Pu, K.; Duan, H. Compact Plasmonic Blackbody for Cancer Theranosis in the near-Infrared Ii Window. *ACS Nano* **2018**, *12*, 2643−2651.
(78) Bowman, R. W.; Gibson, G. M.; Linnenberger, A.; Phillips, D. B.; Grieve, J. A.; Carberry, D. M.; Serati, S.; Miles, M. J.; Padgett, M. J. Red Tweezers": Fast, Customisable Hologram Generation for Optical Tweezers. *Comput. Phys. Commun.* **2014**, *185*, 268−273.
(79) Mohsen-Nia, M.; Modarress, H.; Rasa, H. Measurement and Modeling of Density, Kinematic Viscosity, and Refractive Index for Poly(Ethylene Glycol) Aqueous Solution at Different Temperatures. *J. Chem. Eng. Data* **2005**, *50*, 1662−1666.
(80) Johnson, P. B.; Christy, R. W. Optical Constants of the Noble Metals. *Phys. Rev. B* **1972**, *6*, 4370−4379.
(81) Baffou, G.; Bon, P.; Savatier, J.; Polleux, J.; Zhu, M.; Merlin, M.; Rigneault, H.; Monneret, S. Thermal Imaging of Nanostructures by Quantitative Optical Phase Analysis. *ACS Nano* **2012**, *6*, 2452−8.
(82) Sun, T.; Teja, A. S. Density, Viscosity, and Thermal Conductivity of Aqueous Ethylene, Diethylene, and Triethylene Glycol Mixtures between 290 and 450 K. *J. Chem. Eng. Data* **2003**, *48*, 198−202.
(83) DiGuilio, R.; Teja, A. S. Thermal Conductivity of Poly-(Ethylene Glycols) and Their Binary Mixtures. *J. Chem. Eng. Data* **1990**, *35*, 117−121.
(84) Kou, Y.; Wang, S.; Luo, J.; Sun, K.; Zhang, J.; Tan, Z.; Shi, Q. Thermal Analysis and Heat Capacity Study of Polyethylene Glycol (Peg) Phase Change Materials for Thermal Energy Storage Applications. *J. Chem. Thermodyn.* **2019**, *128*, 259−274.

https://doi.org/10.1021/acsnano.2c03111
ACS Nano 2022, 16, 10878−10889